Functionally Graded Cathodes for Solid Oxide Fuel Cells

Final Report

Reporting Period: 1 October 2002 to 30 September 2006

DOE Contract No.: DE-FC26-02NT41572
DOE Project Manager: Dr. Lane Wilson

Prepared by

YongMan Choi and Meilin Liu

Center for Innovative Fuel Cell and Battery Technologies
School of Materials Science and Engineering
Georgia Institute of Technology
Atlanta, GA 30332-0245

Report Issued: December 2006

DISCLAIMER

ABSTRACT

This DOE SECA project focused on both experimental and theoretical understanding of oxygen reduction processes in a porous mixed-conducting cathode in a solid oxide fuel cell (SOFC). Elucidation of the detailed oxygen reduction mechanism, especially the rate-limiting step(s), is critical to the development of low-temperature SOFCs (400ºC to 700ºC) and to cost reduction since much less expensive materials may be used for cell components. However, cell performance at low temperatures is limited primarily by the interfacial polarization resistances, specifically by those associated with oxygen reduction at the cathode, including transport of oxygen gas through the porous cathode, the adsorption of oxygen onto the cathode surface, the reduction and dissociation of the oxygen molecule (O_2) into the oxygen ion (O^{2-}), and the incorporation of the oxygen ion into the electrolyte. In order to most effectively enhance the performance of the cathode at low temperatures, we must understand the mechanism and kinetics of the elementary processes at the interfaces. Under the support of this DOE SECA project, our accomplishments included

- Experimental determination of the rate-limiting step in the oxygen reduction mechanism at the cathode using *in situ* FTIR and Raman spectroscopy, including surface- and tip-enhanced Raman spectroscopy (SERS and TERS).

- Fabrication and testing of micro-patterned cathodes to compare the relative activity of the TPB to the rest of the cathode surface.

- Construction of a mathematical model to predict cathode performance based on different geometries and microstructures and analyze the kinetics of oxygen-reduction reactions occurring at charged mixed ionic-electronic conductors (MIECs) using two-dimensional finite volume models with *ab initio* calculations.

- Fabrication of cathodes that are graded in composition and microstructure to generate large amounts of active surface area near the cathode/electrolyte interface using a novel combustion chemical vapor deposition (CCVD) technique.

- Application of advanced quantum chemical calculations to interpret measured spectroscopic information, as well as to guide design of high efficient cathode materials.

TABLE OF CONTENTS

LIST OF GRAPHICAL MATERIALS

INTRODUCTION

Solid oxide fuel cells (SOFCs) have attracted much attention because of their high energy efficiency and excellent fuel flexibility,[1-8] but the cost of SOFC systems is still prohibitive. One effective approach to cost reduction is to reduce the operating temperature to the point where much less expensive materials can be used. However, the interfacial polarization resistances increase dramatically as the operating temperature is reduced, especially the resistances to oxygen reduction at the cathode. Thus, one of the key technical challenges facing the SOFC community is to dramatically accelerate the kinetics for oxygen reduction through rational design of porous mixed-conducting cathodes. Understanding the detailed mechanisms of interfacial reactions remains to be a grand challenge, while the development of SOFC technology has moved forward rapidly in recent years. However, the detailed mechanism of oxygen reduction can be very complicated. This project involves exploration of oxygen reduction kinetics with *in situ* experiments. Modeling of mass and charge transport have been also be used to guide design of experiments and optimization of new cathodes. In addition, quantum chemical calculations have been applied to interpret adsorbed oxygen species on surfaces.

This project has centered on elucidating the reaction mechanism of oxygen reduction on SOFC cathode materials using experimental measurements in conjunction with theoretical calculations (*i.e.*, quantum chemical calculations and continuum modeling). More specifically, the technical objectives include

- To elucidate the mechanism of the oxygen-reduction reaction using *in situ* vibrational spectroscopy and *ab initio* calculations;
- To develop micro-impedance spectroscopy system to discern the reaction mechanisms for oxygen reduction and to elucidate the effect of electrode geometry on overall performance of SOFCs;
- To design and construct an ultra high vacuum system for temperature programmed desorption (TPD) and sticking probability measurements relevant to O_2-cathode interactions;
- To analyze the kinetics of oxygen-reduction reactions occurring at charged mixed ionic-electronic conductors (MIECs) using two-dimensional finite volume models with *ab initio* calculations;
- To determine oxygen permeation rate through dense silver membranes to estimate the oxygen transport rate under SOFC operating conditions;
- To develop a mechanistic understanding of the molecular transformations occurring at an SOFC cathode as molecular oxygen arrives from the gas phase, interacts with the cathode surface, and is eventually incorporated as an ionic species into the cathode surface and the bulk structure of the electrolyte;
- To apply acquired knowledge to rationally develop better performing cathodes for SOFCs.

EXECUTIVE SUMMARY

Infrared emission spectra were recorded using Fourier transform infrared emission spectroscopy (FTIRES) for $Sm_{0.5}Sr_{0.5}CoO_3$ (SSC), $La_{1-x}Sr_xFeO_3$ (LSF), $La_{1-x}Sr_xCoO_3$ (LSC), and $La_{1-x}Sr_xMnO_3$ (LSM) cathode materials as a function of temperature, oxygen partial pressure, and applied potential. Peaks attributed to adsorbed superoxide (O_2^-) and peroxide (O_2^{2-}) ions were observed in the spectra, indicating that during oxygen reduction on these cathodes, the oxygen molecule reduces before dissociating into oxygen atoms. Surface-enhanced enhanced Raman spectroscopy (SERS) was successfully applied to examine Ag-$Sm_{0.5}Sr_{0.5}CoO_3$ (SSC) cathode material prepared by a combustion chemical vapor deposition (CCVD) method. In addition, gadolinia-doped ceria (GDC) and undoped CeO_2 were used to identify adsorbed oxygen species using *in situ* surface Raman spectroscopy and quantum chemical calculations, confirming that the band at 831 cm^{-1} is attributed to peroxide-like oxygen species. Two distinct oxygen bands appeared at 825 and 1131 cm^{-1}, corresponding to peroxo- and superoxo-like species, respectively, when partially reduced CeO_2 was exposed to 10% O_2. Periodic density functional theory (DFT) calculations aided the interpretation of spectroscopic observations. An atomic force microscope (AFM) tip was used to enhance the Raman scattering signal of our Raman micro-spectrometer. The tip-enhanced Raman scattering (TERS) effect has increased the sensitivity of the Raman system to analyze the surface of our candidate cathode materials. To calculate oxygen reduction kinetic parameters on an SSC pellet, rapid scan time-resolved spectroscopy (TRS) with Fourier transform infrared (FTIR) was utilized by changing the atmosphere from 100% O_2 to 1% O_2.

Patterned platinum electrodes were fabricated with feature sizes varying from 2-100 μm on yttria-stablized zirconia (YSZ) substrates. The patterned electrodes were tested using electrochemical impedance spectroscopy (EIS). Patterned lanthanum strontium manganese oxide (LSM) electrodes were fabricated with a 2μm feature size on YSZ substrates. The patterned electrodes were tested using EIS. The characteristic thickness at 700°C for dense lanthanum strontium manganese oxide (LSM) was found to be 0.36μm. Above 0.36μm, ionic diffusion is sufficiently difficult such that oxygen ion transport through the LSM electrode is essentially negligible. Beyond this point the surface of LSM electrodes cannot be effectively used and the behavior of the electrode is determined largely by the triple-phase boundaries (TPBs) of the electrodes. In addition, our patterned electrodes were applied to various experiments in this project such as *in situ* spectroscopic tools.

Successfully created electrodes with compositional and structural gradients by changing precursor composition and needle size in our combustion chemical vapor deposition (CCVD) system. The cathode consisted of three porous layer structures, with about 5μm thick 60 wt.% LSM–40 wt.% GDC fine agglomerates (0.5μm diameter) at the bottom (close to YSZ electrolyte), followed by 5μm thick 30 wt.% LSM–30 wt.% LSC–40 wt.% GDC fine agglomerates (0.5μm diameter), and topped with 15 μm thick 60 wt.% LSC–40 wt.% GDC coarse agglomerates (2-3μm diameter) on the air side.

An LSM microelectrode generated from a patterned LSM electrode was used to examine the electrode-geometry effect using micro-impedance spectroscopy. Oxygen permeation through dense silver membranes was determined to follow an Arrhenius relation with an activation

energy of 0.94 eV (21.7 kcal mol^{-1}). The effective leaking current density was calculated to be 0.0146mA cm^{-2} at 750°C.

Regarding theoretical modeling, our continuum modeling showed that a thickness of 0.06 μm is the lower cathode thickness limit for LSM as the sheet resistance becomes unreasonably high below this point. For a particular geometry, similar studies as this one can be performed and the percent utilization can be calculated for all the geometries. Elementary reaction pathways on platinum cathode material were examined to apply to both platinum and MIEC cathode materials, analyzing experimental impedance spectra. In particular, a numerical finite volume scheme was devised to solve a nonlinear DC polarization problem for mixed conductor thin films in two dimensions, including the effect of sheet resistance.

EXPERIMENTAL

Fourier transform infrared emission spectroscopy (pd-FTIRES): Figure 1 shows a schematic diagram of the optical configuration used for the emission measurements.[9] The spectroelectrochemical cell was placed on the top of the sample cup in a Praying Mantis™ diffuse reflectance sampling accessory equipped with a high temperature reaction chamber. The Praying Mantis attachment was positioned at an emission port on the Bruker Equinox 55 FTIR spectrometer. The top surface of the electrode ($0.13cm^2$) then becomes the source of infrared light modulated by the interferometer. While the transfer optics are not perfectly optimized, the electrode surface is at the focal point of the ellipsoidal optics in the diffuse reflectance attachment and the *f* number for the focusing mirror in the emission port is small, therefore light levels reaching the detector are high enough for high quality spectra.[10]

Raman spectroscopy: Details of the experimental setup are shown in Figure 2. All Raman measurements were taken by a Raman microscope (Reinshaw RM1000) with a 1800 line/mm diffraction grating and a CCD detector using a 488 nm Ar ion laser source (Melles Griot). For *in situ* measurements for oxygen specie, a variety of samples such as cathode materials and cerium oxide powder (~0.3 g) was pressed into a pellet of 10mm diameter, placed inside the atmosphere- and temperature-controlled sample chamber (special order, Harrick Scientific), and purged for four hours with Ar (Airgas, UHP grade) at approximately 673K. Then, samples were reduced through exposure to 5% H_2 balanced with Ar at the same temperature. The samples were cooled to room temperature under a flow of Ar before exposing the pellet to 10% O_2 balanced with Ar (Airgas, UHP grade). The surface-treatment process for partial reduction plays a significant role in the observation of adsorbed species, especially peroxo-like species.[11-13] Isotope-substitution experiments with a 10% $^{18}O_2/^{16}O_2$ mixture balanced with Ar (Isotec, > 92% $^{18}O_2$) were carried out to verify surface adsorbed oxygen species.
In addition, our Raman spectroscopy was used with additional surface- and tip-enhanced methods (SERS and TERS, respectively).

Oxygen permeation measurements: Polycrystalline silver foil samples (Alfa Aesar, 99.9%) were stamped and sealed to an alumina tube using both ceramic (Autostic ceramic cement) and metallic (Haraeus, silver conductor paste) seals. The tube-mount setup was mounted in a vertical clam-shell furnace (Applied Test Systems, ATS) and heated to 1073K (see Figure 3). The driving force for oxygen permeation was the chemical potential difference between the ambient atmosphere in the furnace and the inert atmosphere provided by Ar flowing at 75 sccm into the alumina tube. After flowing Ar for 20min, the system was evacuated by using a vacuum pump for 2hr to remove residual species, and then attached to a mass spectrometer (Hiden Analytical, HPR20). The mass spectrometer was used to scan effluent gases from 1 – 50amu at 100 samples per amu, in order to detect oxygen and other oxygen-containing species. Three repetitions of permeation experiments were conducted from 1073 – 723K in 50K increments using Ar flow rates from 20 – 120sccm. The flow rate was controlled by a rotometer (Omega, FL-5GP), which was calibrated to Ar. All effluent gas collected by the mass spectrometer was heated to a temperature above 433 K to prevent condensation and mixing of gaseous species. This helped ensure that oxygen species (monatomic and molecular) present due to permeation through the silver membrane remained in that form and did not combine with other gaseous species (*i.e.*, hydrogen and carbon). A cold cathode

pressure gauge in the UHV housing was monitored to remain constant pressure throughout the experiments.

Combustion CVD: A combustion chemical vapor deposition (CCVD)[14] system (see Figure 4) has been designed and constructed in our laboratory capable of producing nano-particles and nanostructured electrodes or interfaces of various materials. We found that particle size and porosity can be readily controlled by adjusting deposition parameters, such as flame temperature, substrate temperature, fuel flow rate, and solution concentration. Our initial study focused on direct deposition of nanostructured electrodes for solid oxide fuel cells. Both cathode and anode were deposited by combustion CVD on a dense electrolyte. Further, CCVD is ideally suited for preparation of nano-sized powers for electrochemical and catalytic applications in SOFCs.

RESULTS AND DISCUSSION

Fourier Transform Infrared Emission Spectroscopy (FTIRES). Figure 5(a) shows a typical series of emission spectra of an SSC cathode as the atmosphere switches from argon to 1% oxygen. As the sample is exposed to an oxygen-containing environment, the baseline shifts from horizontal to curved, and a series of peaks emerge from the baseline. For purposes of clarity, the spectra obtained as the atmosphere was switched from 1% oxygen back to argon have been omitted; however, the baseline does indeed reverse from curved back to horizontal, and the peaks in the 800 to 1250cm^{-1} region slowly disappear. The baseline shift has been attributed to changes in the properties of the bulk electrode material and will be analyzed at a later time. The spectral features from 1400 to 1800cm^{-1} and from 2300 to 2500cm^{-1} are common to water vapor and carbon dioxide and thus result from random fluctuations in the carbon dioxide and water vapor concentrations between the emission sample chamber and the FTIR detector. The only peaks that related directly to the change in atmosphere were those located between 800 and 1250cm^{-1}. The peaks at approximately 1236 and 1124cm^{-1} were assigned to adsorbed superoxo-like (O_2^-) species while the features around 930cm^{-1} were attributed to adsorbed peroxo-like (O_2^{2-}) species. The presence of the reduced oxygen molecular species on the surface demonstrates that for oxygen reduction on this cathode material, the adsorbed O_2 molecule is reduced before it dissociates. Further, since the reduced oxygen species are observable on the surface, the rate-limiting step for this mechanism is not the initial reduction of O_2. Further studies are necessary to discern which step after the initial reduction is the exact rate-limiting step.

To quantify the concentration of adsorbed oxygen species on the surface, the height of the 1124 cm^{-1} superoxide peak was calculated by subtracting away the curved baseline. Figure 5(b) shows the change in the 1124cm^{-1} peak intensity as the atmosphere was switched from pure argon to 1% O_2 for five minutes and then back to argon for SSC, LSF, and LSC at 600ºC. SSC had the greatest intensity, indicating the largest concentration of surface species and thus the greatest amount of oxygen reduction activity of the three materials. This result is consistent with electrochemical performance data of the three materials under similar operating conditions. This time-dependent data is being further analyzed to obtain kinetic parameters of the oxygen reduction mechanism, which can be used for our mathematical modeling of the system.

The use of rapid scan time-resolved spectroscopy (TRS) in conjunction with our FTIR emission spectroscopic studies has allowed us to refine the time-dependent FTIR data being used to determine experimentally oxygen reduction kinetic parameters. By taking emission spectra on a smaller time scale, we have been able to isolate changes in the cathode's emissivity that are due to small changes in sample temperature from those that are due to structural changes in the material. By subtracting out the thermal effects, we can now more confidently calculate the surface reaction rate and bulk diffusivity of the cathode using FTIR emission spectroscopy.

Raman Spectroscopic Measurements. SERS has been used to examine the bulk cathode material and atomic and molecular species adsorbed on the cathode surface. Shown in Figure 6(a) are enhanced Raman spectra under various atmospheres for composite cathode material

Ag-SSC (SSC 50 wt.% and Ag 50 wt.%) prepared by CCVD. The SERS study gave two new vibration modes at 594 and 1170 cm^{-1}. In particular, to test the validity of the computational methods being used for interpreting the experimental data, especially for adsorbed oxygen species, a simpler material system was chosen. Cerium oxide (CeO_2) was chosen because (1) its AO_2 fluorite structure is a simpler lattice than the defective ABO_3 perovskite structures of typical SOFC cathode materials and (2) it has a well-studied Raman spectra, electronic structure, and defect chemistry. Figure 6(b) compares the Raman spectrum of a nanocrystalline ceria pellet before and after exposure to oxygen after being reduced in 5% hydrogen. After exposure to $^{16}O_2$, a new peak appeared at 831cm^{-1}. To confirm that this peak was indeed an oxygen-containing species, another Raman spectrum was recorded after exposing the pellet to 10% $^{18}O_2$ (balance argon) for 15 minutes (also shown in Figure 6(b)). The peak shifted from 831cm^{-1} to 781cm^{-1}. The ratio between the two peak positions is 1.06, which is the ratio expected for a change from ^{16}O to ^{18}O (i.e., $\sqrt{18/16} = 1.06$), confirming the band at 831 cm^{-1} is attributed to an adsorbed oxygen species. Further, interactions between O_2 and CeO_2 were examined experimentally by *in situ* Raman spectroscopy and theoretically by density functional slab model calculations. In addition, to detect a band attributed to superoxo-like species, we used a different size of cerium oxide powder (Sigma-Aldrich, average particle size = 10 – 20 nm). As illustrated in Figure 7(a), when partially reduced CeO_2 was exposed to 10% O_2, two distinct oxygen bands appeared at 825 and 1131cm^{-1}, corresponding to peroxo- and superoxo-like species, respectively. In order to verify the peaks were indeed an oxygen-containing species, another Raman spectrum was recorded by exposing the sample to 10% $^{18}O_2$ and observing any shift in peak position as discussed above. The small shift from 781 to 778 cm^{-1} may result from different particle sizes. Periodic density functional theory (DFT) calculations based on the surface mode shown in Figure 7(b) aided the interpretation of spectroscopic observations and provided energetics and geometrical information for the dioxygen species adsorbed on CeO_2. Among the surface models, in order to avoid the boundary effects of the cluster approach and to mimic metal oxides, the periodic slab-model framework has been applied to characterize O_2-surface interactions.[15-17] For the exchange and correlation energies, generalized gradient approximation (GGA) such the Perdew-Wang (PW91) functional was used. The calculations were carried out using proper Monkhorst-Pack mesh[18] **k**-points and with a cut-off energy. The slabs were separated by a vacuum spacing greater than 15 Å to ensure no interaction between slabs. Moreover, in order to provide a scientific basis for experimental vibrational spectroscopic data, vibrational-frequency calculations for adsorbed oxygen species can be applied in the harmonic oscillator approximation. It is well-known that mapping out minimum energy paths (MEPs) is imperative to elucidate the most probable reaction pathways. The adsorption energy is calculated according to the following equation. $\Delta E = \Sigma E[\text{products}] - \Sigma E[\text{reactants}] = E[\text{substrate + adsorbate}] - E[\text{gas-phase } O_2 \text{ molecule}] - E[\text{substrate}]$. The O_2 adsorption energies on unreduced CeO_2 surfaces are unstable, while those on reduced surfaces are exothermic ($-4.0 < \Delta E_{ads} < -0.9$ eV), depending on other relevant surface processes such as chemisorption and diffusion into the bulk. Partial reduction of surface Ce^{4+} to Ce^{3+} (together with the formation of oxygen vacancies) can alter geometrical parameters and, accordingly, lead to a shift in the vibrational frequencies of adsorbed oxygen species compared to those on unreduced CeO_2. Moreover, the location of oxygen vacancies affects the formation and subsequent dissociation of oxygen species on the surfaces. DFT predictions of the adsorption

energetics support the experimental observation that oxygen adsorption and reduction is energetically more favorable on reduced ceria surfaces than on unreduced surfaces.

To examine adsorbed oxygen species on cathode materials, nanoparticles of the desired mixed oxides (LSM, LSC, and SSC were deposited on a YSZ substrate using combustion CVD (CCVD). To generate a surface enhanced Raman signal (SERS) effect, silver nanoparticles were deposited simultaneously with the cathode material. Besides having a greater intensity, the SERS spectrum also has more distinct peaks. The key to observing adsorbed oxygen peaks in the Raman spectra – besides having a high exposed surface area – is having a surface sufficiently clear of surface hydroxyl groups and other unwanted adsorbants before exposing the sample to oxygen. We are currently testing various evacuation regiments at different temperatures to find a method that cleans the cathode surface sufficiently enough to generate a detectable adsorbed oxygen species signal. Shown in Figure 8 are the Raman spectra of a thin LSM film with and without the presence of an atomic force microscope (AFM) tip near the film surface. We can see that the presence of the AFM tip the dramatically enhanced the intensity of the Raman scattering signal many new peaks appeared in the spectrum. The two peaks at 860 and 1122cm^{-1} are considered to be surface adsorbed peroxide and superoxide species. Further investigations into these tip-enhanced Raman scattering (TERS) spectra should yield valuable information about the exact structure of the cathode surface.

Patterned Electrodes Fabricated by Photolithography and PLD. We have succeeded in depositing both platinum and LSM patterned electrodes on YSZ substrates of varying feature size. By reducing the feature size, the amount of TPB can be increased rapidly while maintaining the same amount of surface area. Figure 9(a) shows an SEM micrograph of patterned electrode lines 2μm in width. This resolution is critical to accurately quantify the TPB length dependence of cathode performance. The cathode/electrolyte interfacial resistance was calculated from the characteristic impedance loops shown in Figure 9(b). Figure 9(c) shows the interfacial conductance (the inverse of the resistance) plotted as a function of the TPB length. This figure demonstrates the expected trend that as the relative amount of electrochemically active area (the TPB) increases with respect to total surface area, the conductivity of the electrode also increases. An expected plateau of LSM impedance at large TPB lengths was not accurately resolved, indicating that for a predominately electronic conductor such as LSM, the active region of the TPB extends less than 1μm from the TPB itself. One micron is half of the current minimum possible feature size. Process parameters are being developed to fabricate LSM electrodes with sharply reduced feature sizes through the use of electron-beam lithography.

To quantify the effect of electrode thickness on the performance of dense LSM electrodes, we fabricated patterned electrodes. The electrode array consisted of 60 patterned rectangular electrodes 40 μm in width separated by 60μm gaps. A platinum current collector was lithographically patterned and deposited on top of the working electrode. The current collector consisted of 12 identical 50μm wide platinum strips separated by exactly 490 μm. All 12 platinum strips were connected to a platinum pad in order to facilitate wire attach.(see Figure 10(a)). Figure 10(b) displays the dependence of the interfacial impedance on the electrode strip thickness at 700 and 750^{o}C. Several unique traits are observed in each temperature range. In particular, note the peak conductance, located between 0.18 μm and

0.22 μm, followed by a rapid decay with increasing thickness. It should also be noted that the decay behavior appears to asymptotically approach a non-zero value. This value, believed to be about $0.012\Omega^{-1}$, has been attributed to standardized factors within the cell. Among these are the TPB and surface transport contributions of the LSM array as well as the catalytic contributions of the platinum current collector. Since these factors have been systematically controlled through the design and fabrication stages, their contributions should be constant over the entire range of electrode thickness. Consequently, the background noise value can be subtracted from the overall conductance to yield the contribution merely from a pathway depending upon bulk transport through the dense MIEC.

Combustion Chemical Vapor Deposition. Shown in Figure 11 (a) is a cross sectional view (as fractured) of a half-cell with composite cathode supported by a 240 μm thick dense YSZ electrolyte. The cathode fabricated by combustion CVD consists of three porous layer structures and is graded in both microstructure and composition, with about 5 μm thick 60 wt.% LSM–40 wt.% GDC fine agglomerates (0.5μm diameter) at the bottom (close to YSZ electrolyte), followed by 5μm thick 30 wt.% LSM–30 wt.% LSC–40 wt.% GDC fine agglomerates (0.5μm diameter), and 15 μm thick 60 wt.% LSC–40 wt.% GDC coarse agglomerates (2-3μm diameter) on the top (air side). The two bottom layers are actually nanostructured as shown in the inset Figure 11 (b), offering extremely high surface area for oxygen reduction. Energy dispersive spectroscopy (EDS) dot mapping revealed the compositional changes on the cross sectional micrograph. As shown in Figure 11(c), manganese content gradually declined from YSZ/LSM–GDC interface to LSC–GDC airside, while the cobalt signal exhibited the opposite trend as shown in Figure 11(d). The manganese-rich layers provide fast electrochemical reaction rates, high chemical stability, and a satisfying match in thermal expansion coefficient with YSZ electrolyte. Meanwhile, the large interconnected pore channels within the coarse top layer facilitate oxygen gas mass transport through the cathode. The cobalt-rich top layer has high conductivity for efficient current collection.

Micro-impedance Spectroscopy. Shown in Figures 12(a) and 12(b) are typical SEM images of a WC tip used for current collection and an LSM microelectrode (ME) generated from a patterned LSM electrode using an electrochemically etched tungsten-carbide tip, respectively. The height and width of the LSM patterned electrode and the space between two adjacent LSM electrodes are 0.8, 11.5, and 20μm, respectively. The rest of the patterned LSM electrodes were used as the counter electrode (CE). By controlling the position of the LSM microelectrode, we can separate the ME and CE by a single YSZ grain boundary, or put the ME and CE onto a single YSZ grain. Shown in Figure 12(c) is the effect of the LSM ME perimeter on LSM-YSZ interfacial impedance at 650°C. It was found that the Ohmic portion of the impedance decreased as the perimeter of the LSM ME was increased. In addition, we found that the product of the ME perimeter and the Ohmic portion of the impedance also decreased with an increase of the ME perimeter. The product should remain constant if TPBs are single lines around the ME. It seems that the small ME has a larger perimeter specific resistance as compared to the larger perimeter ME's. A possible explanation is that some unobservable delamination caused by the scratching process has occurred. The smaller the ME, the higher the relative percentage of delaminated area and thus, the larger the Ohmic portion of the impedance resistance. The proposed delamination issue could be resolved by

scratching the patterned ME before the annealing process. Specifically, after the patterned electrode was fabricated by the sputtering process, the ME would be scratched, and then annealed at higher temperature. Another observation was an increase in the impedance with increased DC bias, suggesting the electrode reaction is mass transfer limited. Application of DC bias should not change the shape of the impedance spectrum, as the DC bias should only influence the non-ohmic component. After applying DC voltage, the impedance was collected without DC bias again. No significant change was found indicating that application of DC bias did not damage or alter the ME. More detailed studies to interpret the experimental observations with an electrochemical modeling are in progress.

Oxygen Permeation through Ag. As illustrated in Figure 13, oxygen permeation through dense silver membranes was determined to follow an Arrhenius relation with an activation energy of 0.94eV (21.7kcal mol^{-1}), which is comparable to literature values. The quantitative oxygen permeation and flux were also in agreement with reported values from the literature. Though oxygen permeation rates increased with temperature, the effective leaking current density generated at high temperatures (0.0146mA cm^{-2} at 750°C) is still minimal enough to allow silver to meet the gas separation requirements for SOFC materials. Similar to what has been found in previous literature, degradation of the silver surface was observed to occur at the grain boundaries after only a few hours. A silver layer of about 12μm (deposited by DC sputtering) was sufficient to prevent a quantifiable oxidation front within the Ni-YSZ anode after 8-hour exposure to SOFC operating conditions, nevertheless significant surface porosity was still observed. As silver theoretically makes a viable SOFC interconnect material for intermediate- and low-temperature SOFCs, the study on the grain boundary degradation will be examined in more detail for successful application.

Continuum Modeling: Shown in Figure 14(a) is the configuration of the full-scale electrode system used for modeling study of the patterned electrodes. The current collector is placed as the topmost layer and has 11 stripes. The stripes are connected at one end. The gap between each pair of successive stripes is 490μm. The electrode bars are in 60 parallel rows below this layer. The bottom-most layer is the electrolyte (substrate). As illustrated in Figure 14(b), the sheet resistance shoots up at small feature sizes (i.e., below 0.18μm), whereas the interfacial resistance trend reverses. Electrode thicknesses below 0.18μm show tremendous ohmic losses as the sheet resistance (i.e., via the electronic conductivity) dominates the performance and the entire electrode may no longer be assumed utilized at 100%. The outcome of the sheet resistance calculations may in turn be used to make necessary corrections and help remake the design of the patterned electrodes. In addition, this work clears up some confusing behavior previously observed on thin film LSM electrodes, wherein polarization resistance initially decreases with thickness for very thin films but then increases again as thicknesses grow beyond a threshold value. The need for systematic guidance towards fabricating patterned electrodes of optimum geometry motivated this research. While patterned LSM electrodes were used for this model study, our proposed computational approach is applicable to any patterned electrode.

Reaction mechanisms have been developed to describe the oxygen reduction process occurring at the MIEC cathode materials. Experimental impedance measurements typically include a double layer capacitance, C_{dl}, and a resistive element attributed to the electrolyte, R_e.

These additional elements obscure the Faradaic impedance of the system, Z_F. To be able to more directly compare experimental data and theoretical calculations, a method was used to determine the total impedance from knowledge of the Faradaic impedance. From knowledge of the electrolyte resistance and the double layer capacitance, values for the total electrode impedance were computed. Illustrated in Figure 15 are the results comparing total impedance to Faradaic impedance, in which the total impedance can quickly show the electrolyte resistance and the polarization resistance, but hides the charge transfer resistance, R_t

We have developed a model to predict the electrochemical response of thin-film and patterned electrodes, which we then used to account for sheet resistance in LSM thin films for a 60nm thick with current collectors 50μm apart. We found that electrical potential increases along the length of the film between current collectors due to sheet resistance. Shown in Figure 16 is a simulated, normalized cathodic I-V curve for the film. Note the Tafelian behavior in Figure 16. The semi-log scale in the left-hand plot of the figure reflects the shape of a co-limited process. In this case, the limiting factors are ionic transport at low overpotentials, and sheet resistance at high overpotentials. The reason for the switch is that the vacancy transfer at the interface is potential-dependent, with an exponential response to potential changes (hence the Tafelian profile), while bulk electronic transport is only linearly responsive to potential. A greater concentration of vacancies in the bulk leads to higher ionic conductivity, in turn leading to greater sheet resistance losses. The problem is a difficult one to solve, since consideration of sheet resistance obviates the common assumption of ambipolar diffusion in MIECs, which simplifies the mathematics considerably but will not always be true for thin films. In addition, the problem is in two dimensions and is nonlinear. A numerical finite volume scheme was devised to solve the problem. The scheme used is time-dependent (even though the model results prior to steady-state are not reliable), since that enables the use of a linear solver. This scheme works quite well at low overpotentials, however at cathodic overpotentials above 500mV, the method slows down and ultimately becomes unstable. However, the instability in the numerical solver we have found so far is limited to high potential regions in which the material itself would not be chemically stable in reality.

CONCLUSIONS

Under the support of this SECA project, we made important progress in elucidation of the mechanism of oxygen reduction on cathode materials for SOFCs by means of experimental and computational approaches.

Classical kinetic analysis for a simple breakdown of the reaction occurring at the gas exposed surface on MIECs results in a set of equations that depend on changes in the surface potential in an exponential fashion, implying that the nature of the reactions is electrochemical in general. However, the effect of surface potential is opposite for adsorption and incorporation steps, requiring that chemical driving forces play a dominant role at some point in the course of the overall reaction. Whether the reaction is electrochemically or merely chemically controlled therefore depends on the specific mechanism and the identity of the rate limiting step(s). Two-dimensional simulations of MIECs in half-cell configurations show that, for a simple reaction mechanism involving dissociative adsorption and incorporation on the MIEC surface only, the change in surface potential is negligible for an incorporation-controlled mechanism but appreciably negative for an adsorption-controlled one.

The combination of *in situ* vibrational spectroscopy with *ab initio* calculations has provided detailed molecular-level information about surface adsorbed oxygen species. For example, interactions between O_2 and CeO_2 are examined experimentally using *in situ* Raman spectroscopy and theoretically using density functional slab-model calculations. Two distinct oxygen bands appear at 825 and 1131 cm^{-1}, corresponding to peroxo- and superoxo-like species, respectively, when partially reduced CeO_2 is exposed to 10% O_2. Periodic density-functional theory (DFT) calculations aid the interpretation of spectroscopic observations and provide energetic and geometric information for the dioxygen species adsorbed on CeO_2. The O_2 adsorption energies on unreduced CeO_2 surfaces are endothermic ($0.91<\Delta E_{ads}<0.98$ eV), while those on reduced surfaces are exothermic ($4.0<\Delta E_{ads}< 0.9$ eV), depending on other relevant surface processes such as chemisorption and diffusion into the bulk. Partial reduction of surface Ce^{4+} to Ce^{3+} (together with formation of oxygen vacancies) alters geometrical parameters and, accordingly, leads to a shift in the vibrational frequencies of adsorbed oxygen species compared to those on unreduced CeO_2. Moreover, the location of oxygen vacancies affects the formation and subsequent dissociation of oxygen species on the surfaces. DFT predictions of the energetics support the experimental observation that the reduced surfaces are energetically more favorable than the unreduced surfaces for oxygen adsorption and reduction.

The O_2-$LaMnO_3$ interactions were predicted using periodic DFT/MD calculations. It was found that the oxygen reduction can occur via molecular and dissociative adsorption. Surface species on La, Mn, and O_{sub} sites were identified at 0 K as the superoxo- or peroxo-like species based on their estimated geometries and vibrational modes (O-O stretching bands at 1143 – 1265 or 861 – 1017 cm^{-1}, respectively), depending on configurations and computational methods used. However, the loose reaction barriers in the whole process at both perfect and defective $LaMnO_3$ surfaces suggest fast kinetics for oxygen reduction on the surfaces. In particular, it was found that oxygen vacancies influence the oxygen reduction kinetics. The DFT/MD modeling is useful for elucidating the oxygen reduction mechanism at

the SOFC cathode surfaces; these and similar results for other electrode materials may aid in the development of more efficient and cheaper electrodes. Based on our conclusions, it is possible to develop a continuum framework that includes the prediction of partial charges of each possible species and product, which will be applied in subsequent macroscopic modeling. To fully understand the oxygen reduction reaction under the SOFC conditions, further *in situ* spectroscopic and theoretical investigations will explored.

A model for electrochemical response was established to account for the affect of sheet resistance in LSM thin films using a numeric finite volume scheme. A model of the cathodic reaction on thin film MIECs and a comparison with experimental data suggests that sheet resistance can play an important role in the overall cell resistance, becoming more important as polarization increases. A model incorporating the phenomenon was derived, and its finite volume-based numerical solution was stable in two dimensions at most practical overpotentials. Simulations using parameters collected from the literature show an ionic transport limitation at low overpotentials, and sheet resistance at high overpotentials. That these processes seem electrochemically activated is explained by the relationship between the charge transfer process at the electrolyte and ionic transport through the reduction of the MIEC bulk. Comparisons with experimental studies revealed that the model is much more resistive, but the differece is much smaller when compared against a study on epitaxial and near-epitaxial films. The general two-regime linear shape of the I-V curves generated by the model seems to match most of those measured experimentally. The major implication is that current collection must be considered in design of LSM electrodes, especially as length scales decrease.

High-performance nanostructured electrodes for SOFCs have been directly deposited on electrolyte substrates using combustion CVD after overcoming several critical issues such as thermal shocking and control of porosity, crystallinity, and phase purity. The produced electrodes consist of nano-grains of less than 50 nm and exhibit remarkably low polarization resistances (i.e. 1.09Ω-cm^2 at 500°C and 0.17 Ω-cm^2 at 600°C). Also, SOFC electrodes with both compositional and structural gradients were fabricated using combustion CVD and demonstrated even better performance. Further, the original combustion CVD was modified to use solid ceramic particles as "precursor" material, which further simplified the fabrication process.

Dense $La_{0.8}Sr_{0.2}MnO_3$ (LSM) electrodes were patterned by photolithography and fabricated via pulsed-laser deposition on YSZ electrolytes. The electrode arrays varied in thickness while maintaining a constant electrode area and three-phase boundary length. Impedance analysis shows that the interfacial polarization resistance decreases significantly as electrode thickness drops below a critical value, beyond which the top surface of the LSM becomes active for oxygen reduction. However, when the LSM electrodes become too thin, the in-plane sheet resistance of the LSM starts to limit the utilization of the electrodes along their length. The quantification of the characteristic thickness is important not only to intelligent design of practical mixed-conducting electrodes but also to the design of patterned electrodes for fundamental studies. This study has demonstrated the effect of electrode thickness on the performance of dense LSM electrodes. Although LSM is often regarded as a pure electronic conductor, this study has shown that for very thin electrodes, the mixed ionic/electronic

conducting behavior of LSM can be significant. The thinner the dense LSM electrodes, the smaller the resistance to ionic transport through the dense LSM layer and therefore the more active the LSM surface becomes for oxygen reduction. In particular, a characteristic thickness was defined as the thickness at which the interfacial polarization resistance drops below 1/e, or approximately 37%, of its peak value (corresponding to the polarization resistance of the TPBs). For dense LSM, this characteristic thickness was found to be 0.36μm at 700°C. Much greater than 0.36 μm in thickness, ionic diffusion is sufficiently difficult such that oxygen ion transport through the LSM electrode is essentially negligible. Beyond this point the surface of LSM electrodes cannot be effectively used and the behavior of the electrode is determined largely by the TPB's of the electrodes. As expected, the characteristic thickness of an MIEC electrode varies with temperature. For very thin electrodes, the sheet resistance may dramatically reduce the effective utilization of the electrode. When this happens, it may no longer be valid to assume that the entire surface area is active. Computational modeling techniques have been used to demonstrate a corresponding drop in the effective utilization of the cathode with decreasing thickness. On one hand, the critical thickness at which the LSM surfaces become active is important to intelligent design of practical porous mixed-conducting electrodes. On the other hand, the critical thickness at which the sheet resistance becomes dominant is important to the design of patterned electrodes for fundamental studies.

The inert properties of silver over a wide temperature range make it a strong candidate for an intermediate temperature SOFC interconnect. However, silver is known to be a selective conductor of H_2 and O_2, which could potentially lead to cell degradation through fuel mixing. Oxygen permeation was determined to follow an Arrhenius relation with an activation energy of 0.940eV (21.7 kcal mol^{-1}), which is comparable to literature values. The quantitative oxygen permeation and flux were also in agreement with reported values from the literature. Though oxygen permeation rates increased with temperature, the effective leaking current density generated at high temperatures (0.015mA cm^{-2} at 750°C) is minimal enough to allow silver to meet the gas separation requirements for SOFC interconnects. Similar to what has been reported in the literature, porosity forms at the grain boundaries of silver when exposed to a H_2/O_2 dual atmosphere at high temperature. A silver layer of about 12μm, deposited on a Ni-YSZ anode by DC sputtering, was sufficient to prevent a quantifiable oxidation front after 8 hours exposure to SOFC operating conditions. Nevertheless significant surface porosity was still observed within the silver layer. While silver would theoretically make a viable interconnect for intermediate temperature SOFCs, the grain boundary degradation appears too severe for successful application.

While the oxygen reduction processes at an SOFC cathode have been extensively studied both experimentally and theoretically, many fundamental questions regarding the processes still remain unanswered, especially for perovskite-type cathode materials. To achieve intelligent design of new cathode materials, the detailed molecular processes relevant to oxygen reduction must be theoretically predicted using first-principles based computations and experimentally probed or mapped using *in situ* characterization techniques. Further, multi-scale modeling techniques are needed to link these microscopic properties to the electrochemical performance (current-voltage characteristics and impedance spectra) of a component or a cell, which can be directly measured using electrochemical techniques.

Figures

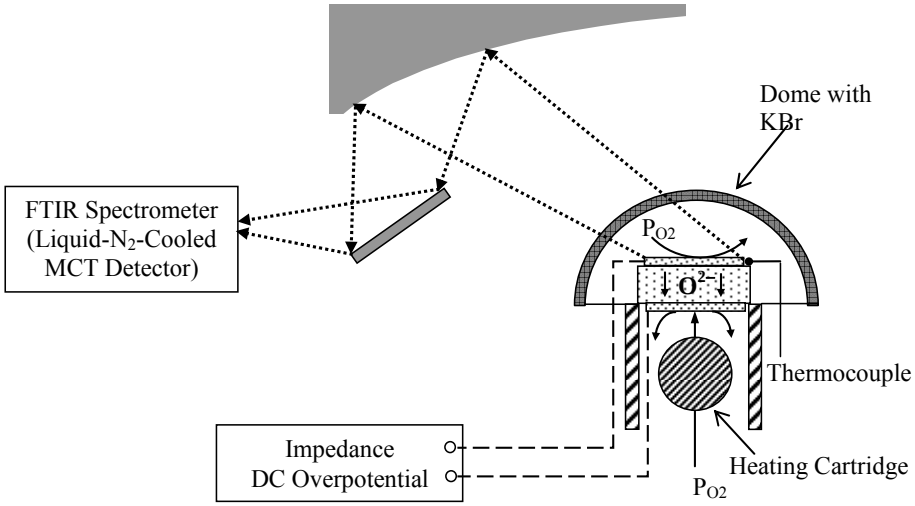

Figure 1. Schematic diagram of optical configuration for pd-FTIRES experiments.

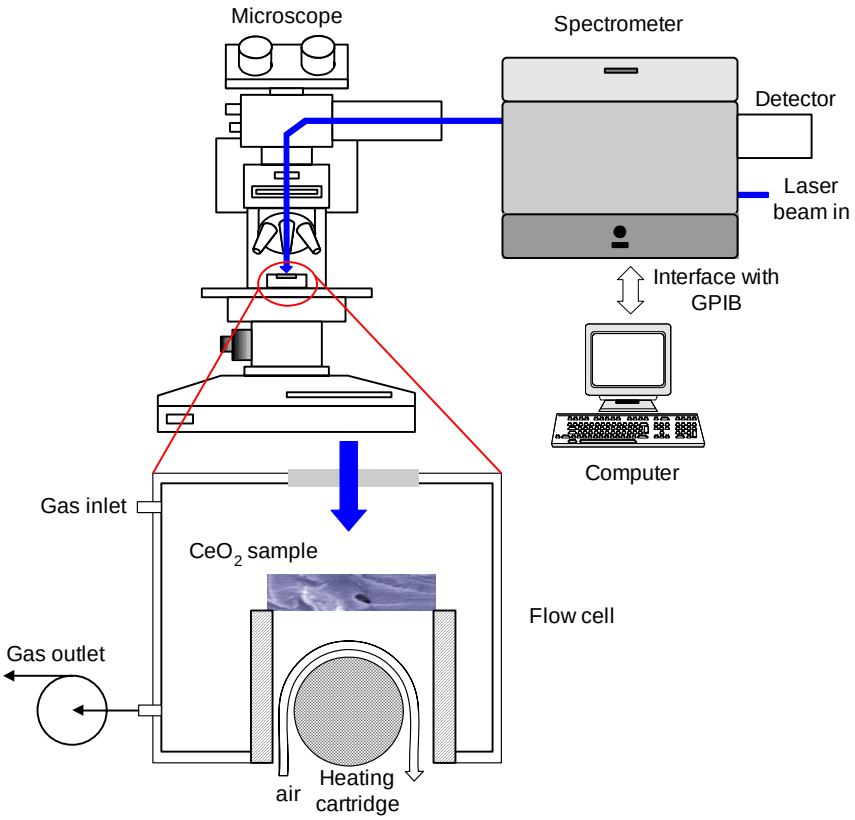

Figure 2. Schematic for *in situ* Raman spectroscopic measurements.

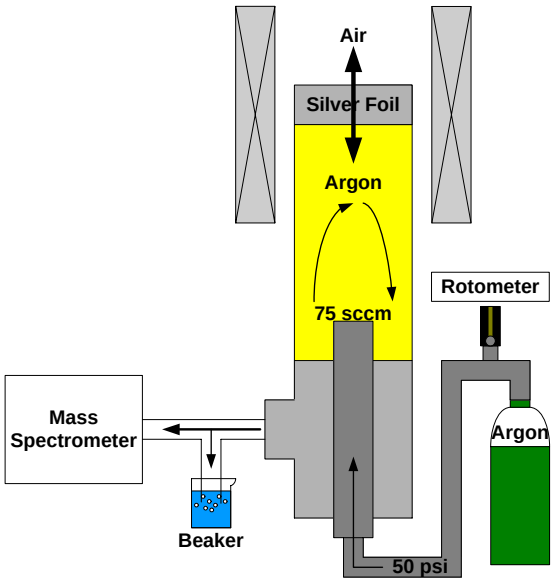

Figure 3. Schematic of system used to measure permeation rate of oxygen through silver.

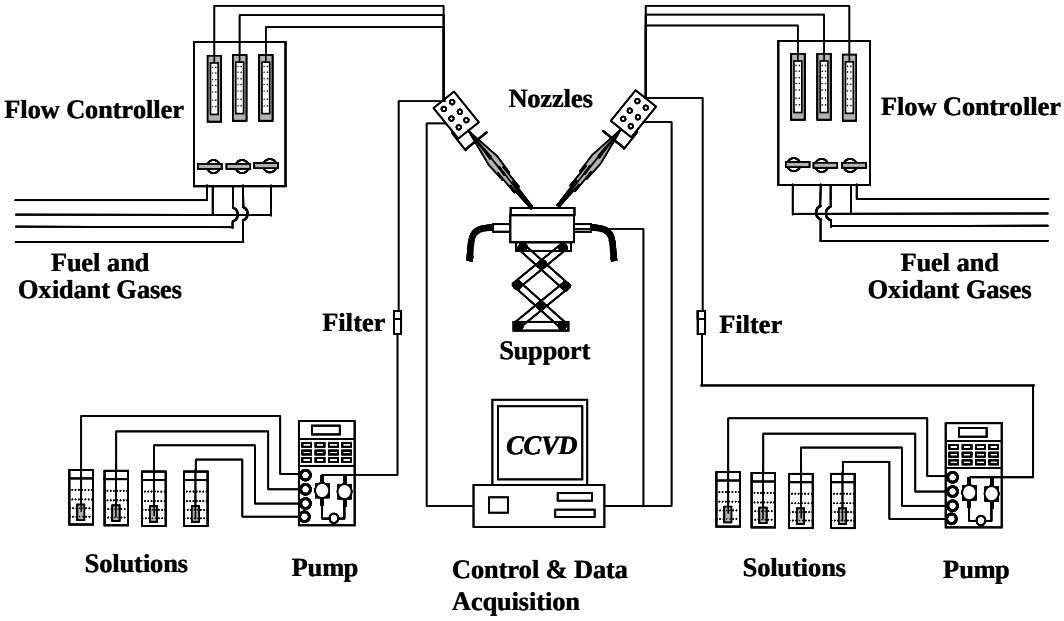

Figure 4. Schematic of Combustion CVD System (CCVD).

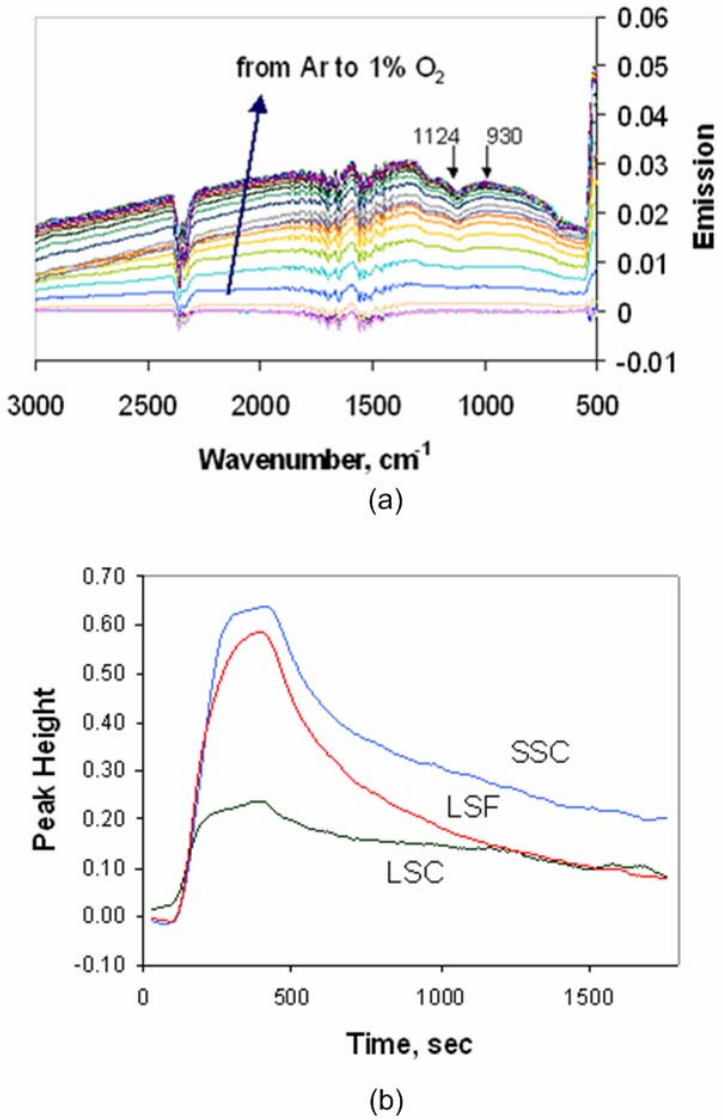

Figure 5. (a) FTIR emission spectra for SSC pellet at 700ºC as sample atmosphere changes from argon to 1% oxygen. All spectra are compared to a background spectrum measured in argon. (b) Plot of the height of 1124cm^{-1} peak during gas switching experiment from argon to 1% O_2 and back to argon for different cathode materials at 600ºC.

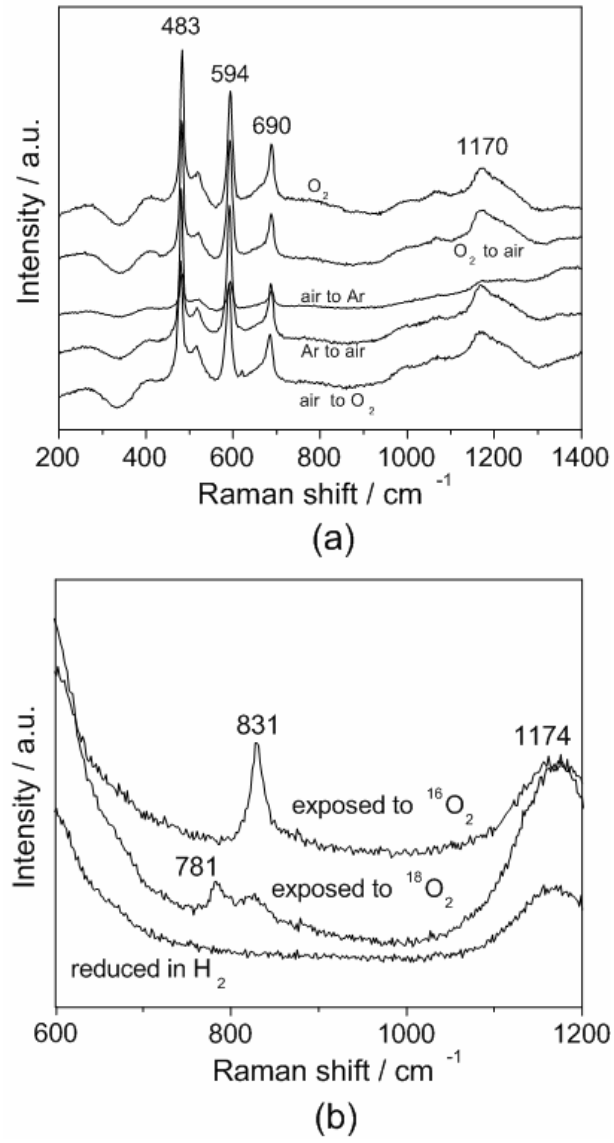

Figure 6. (a) Enhanced Raman spectra for composite cathode material Ag-SSC at 25^{o}C. (b) Raman spectra of CeO_2 nanopowder pellet that had been reduced under 5 % H_2 and then exposed to $^{16}O_2$-and $^{18}O_2$-containing atmospheres.

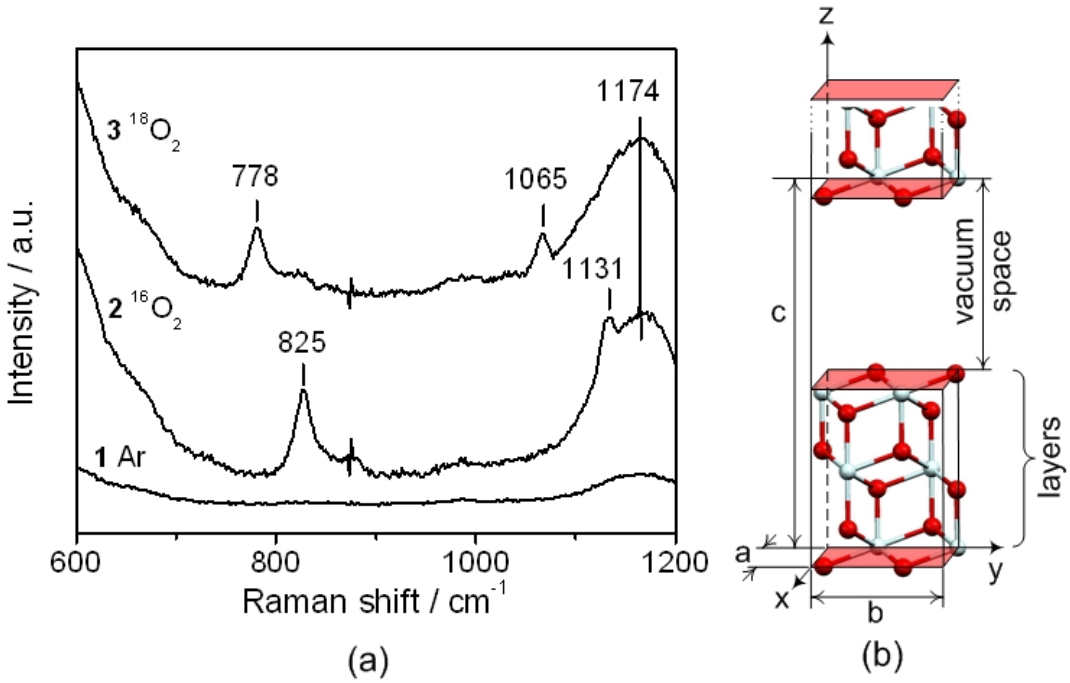

Figure 7. (a) Typical Raman spectra of CeO_2 sample treated by 5% H_2 at 673 K before 298K exposure to (1) Ar, (2) 10% $^{16}O_2$, and (3) 10% $^{18}O_2$ atmospheres (all mixtures are diluted with Ar). (b) A representative surface model with nine layers for the O_2-CeO_2(111) interactions.

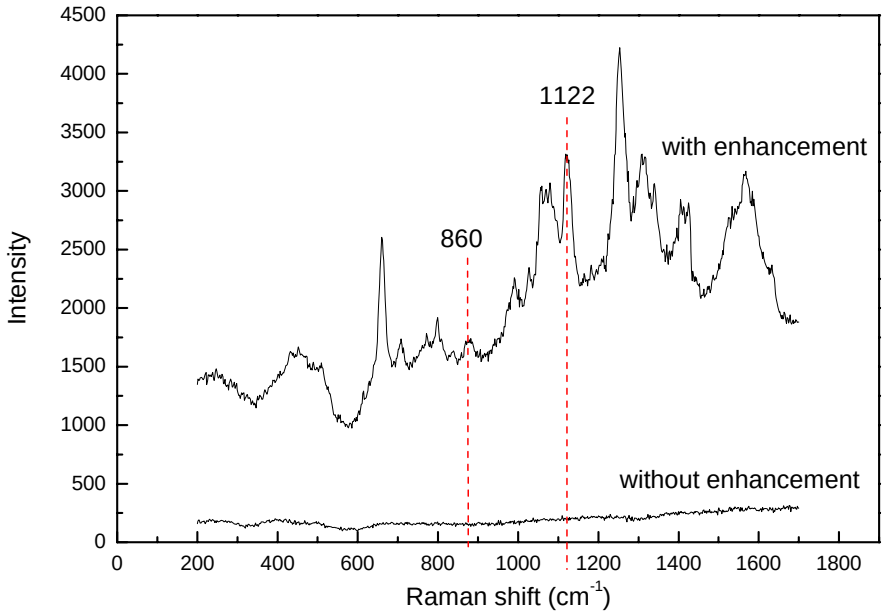

Figure 8. Raman spectra of thin film LSM with and without the tip enhancement.

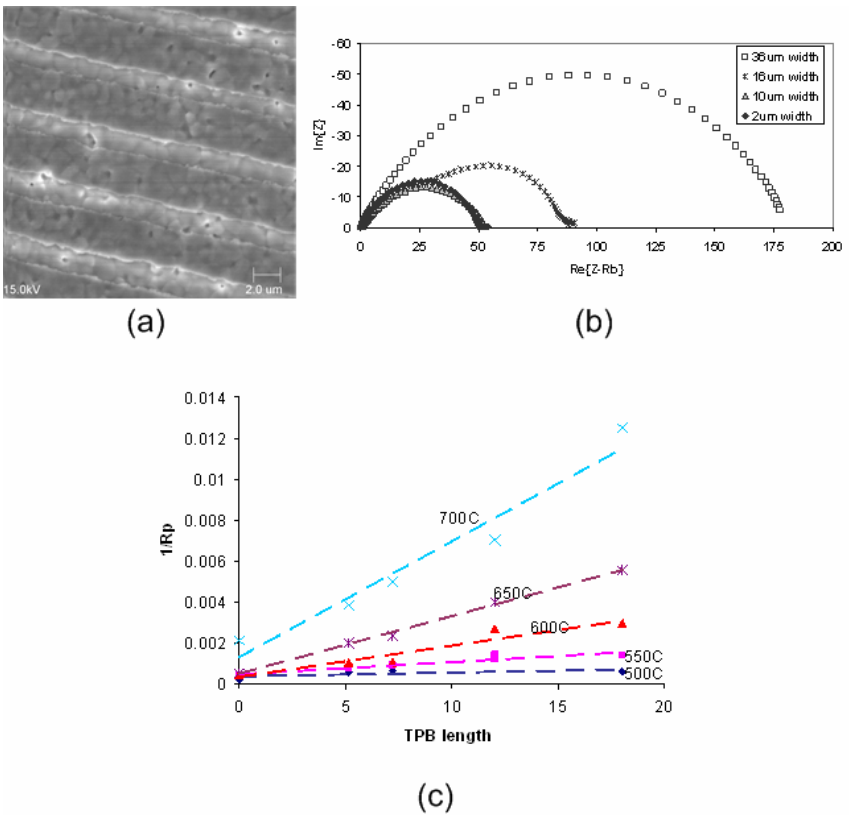

Figure 9. (a) Top view of a patterned LSM electrode with 2μm in width and 0.25μm in thickness. (b) Typical impedance spectra of a patterned LSM electrode at 700ºC. (c) Plot of interfacial conductance versus triple-phase boundary length.

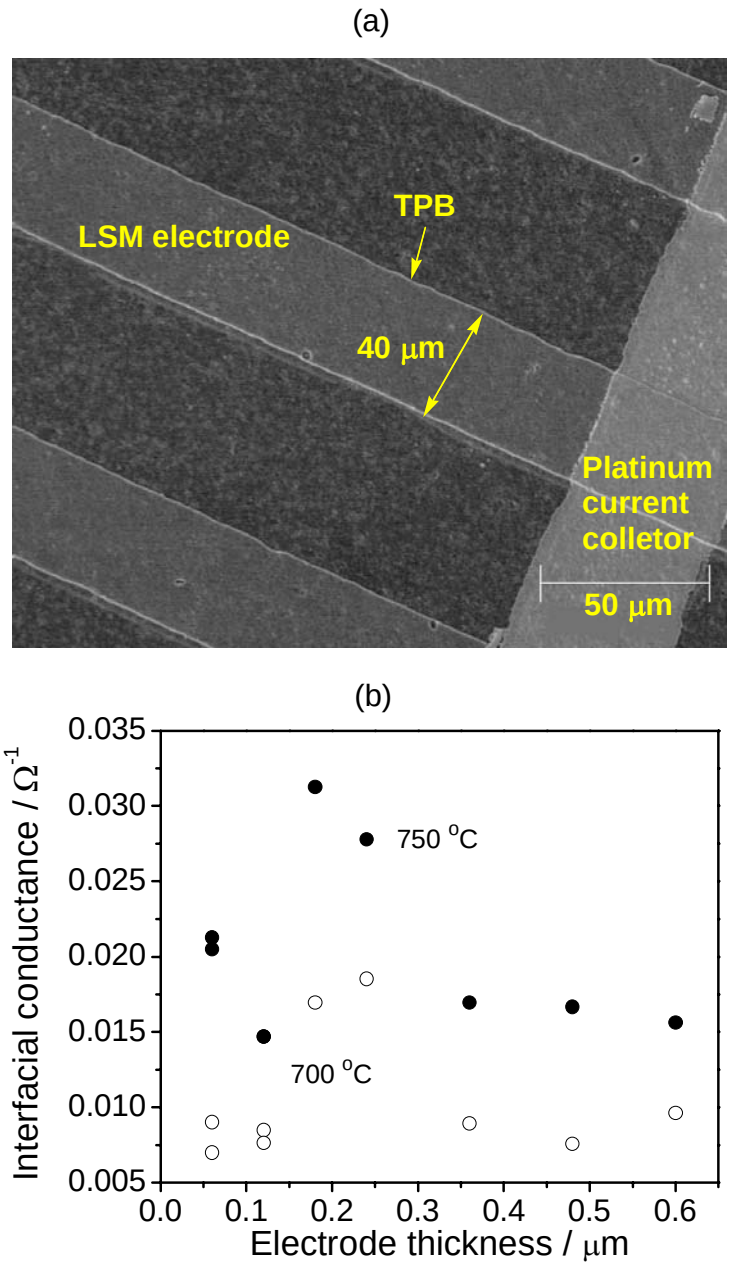

Figure 10. (a) An SEM image of LSM patterned electrodes (with constant TPB length and surface area) on a YSZ substrate. The width of the LSM strip is 40μm and the gap between two adjacent strips is 60μm. Platinum current collector strips run perpendicular to the LSM strips. (b) Plot of the inverse of interfacial resistance.

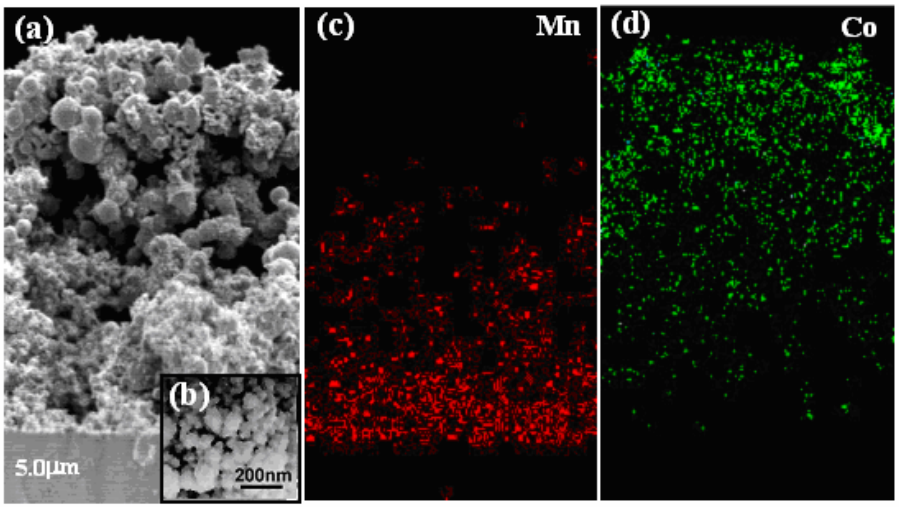

Figure 11. (a) Cross-sectional fracture surface of the functionally graded cathode fabricated on an YSZ pellet using a CCVD process. (b) Higher magnification image of the cathode showing the nanostructure (c) EDS dot mapping showing manganese distribution on the cross-section surface. (d) EDS dot mapping of cobalt distribution.

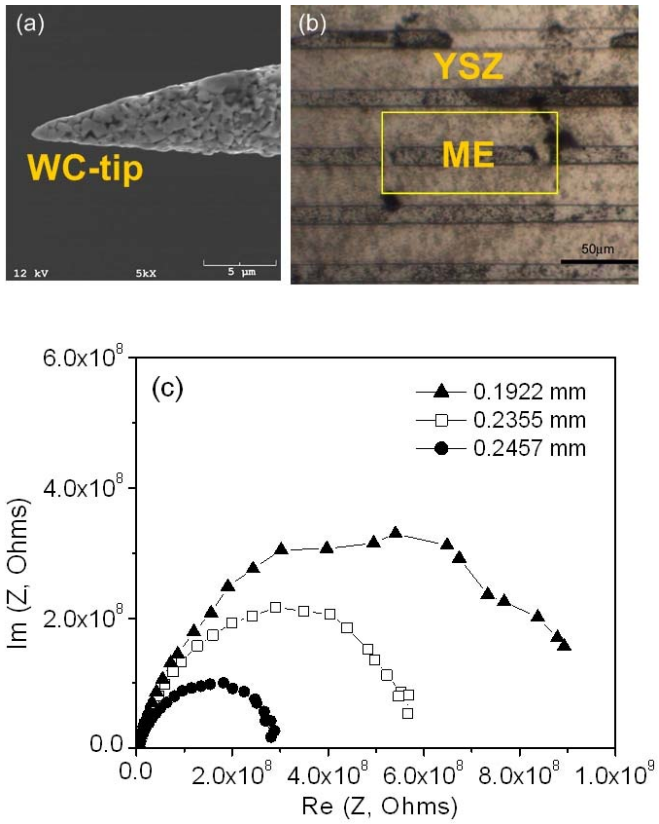

Figure 12. (a) An SEM image of a WC tip used for current collection of ME. (b) An LSM microelectrode generated from a patterned LSM electrode fabricated onto YSZ with large grains. (c) Impedance plots of the LSM microelectrode on YSZ at 650 ^{o}C. The different plots correspond to the different ME perimeters listed in the plot. Note the decrease in overall impedance with increased the ME perimeter.

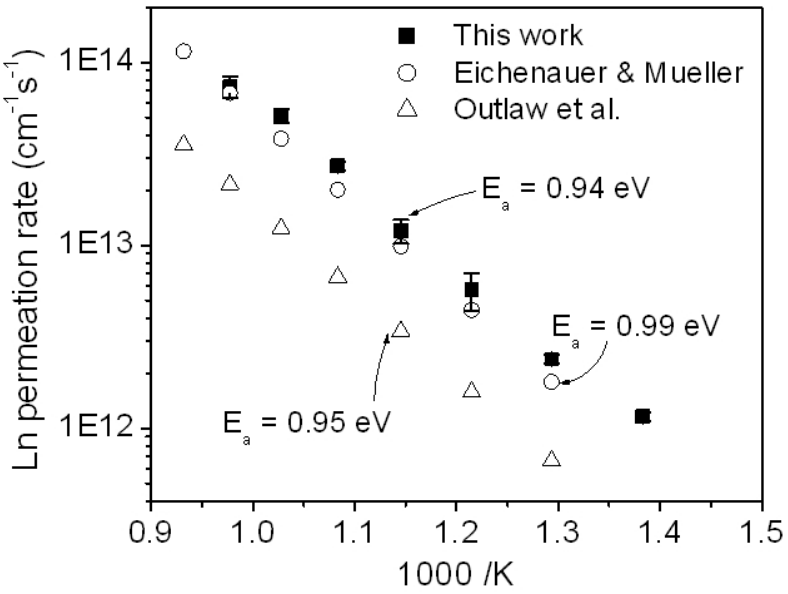

Figure 13. Arrhenius plot of measured oxygen permeation rate through dense silver versus inverse temperature (solid symbols) compared to literature values (open symbols).

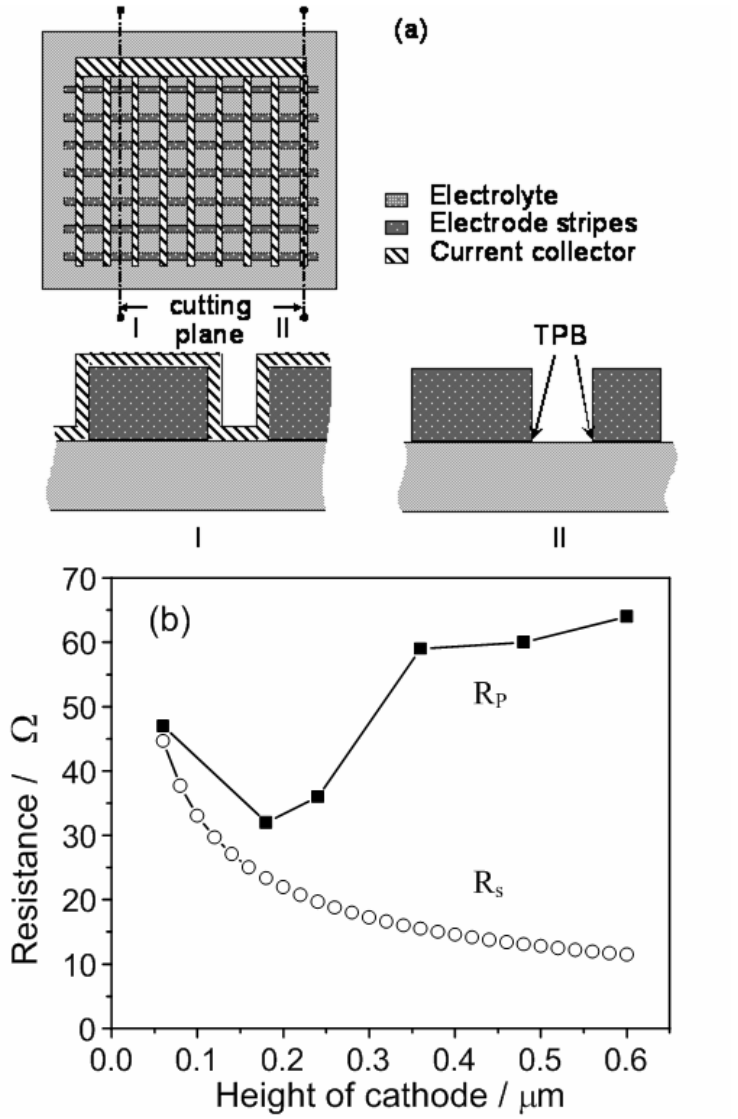

Figure 14. (a) Top and cross-sectional views as seen through the cutting plane (b) Comparative plot of sheet (R_s) and interfacial resistances (R_p) as a function of electrode thickness.

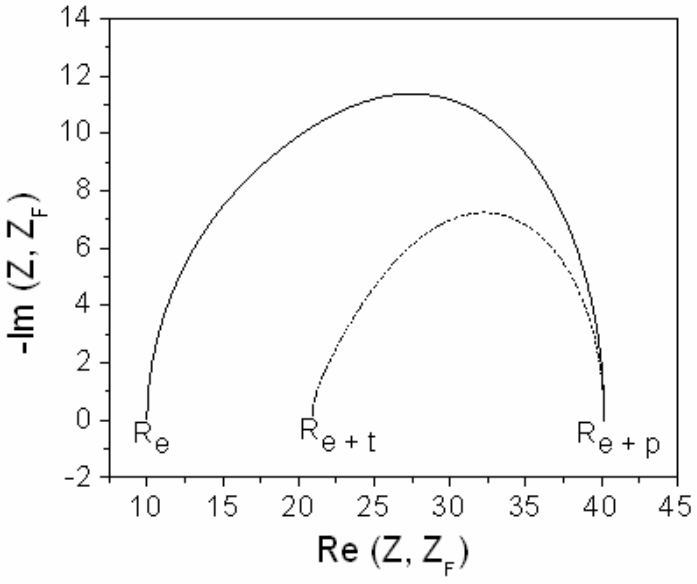

Figure 15. Impedance spectra showing typical calculated total impedance, Z (solid line), and the calculated Faradaic impedance, Z_F (dashed line), responses for a proposed mechanism at T = 700°C, P = 1 atm, R_e = 10 Ω, $C_{dl} = 2\times10^{-6}$ F. R_e, R_t, and R_p correspond to electrolyte resistance, charge transfer resistance, and polarization resistance, respectively.

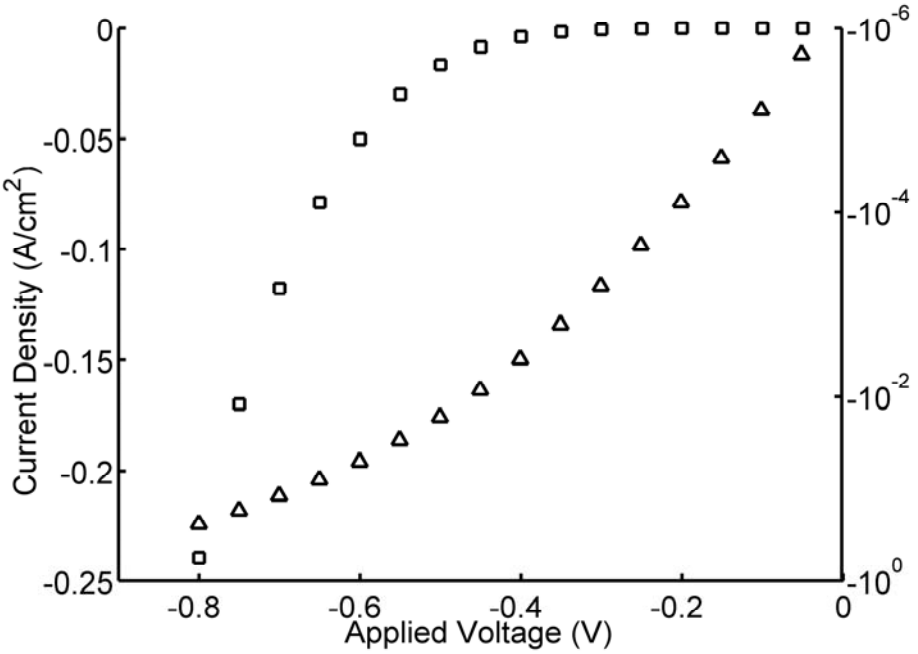

Figure 16. I-V curve for a 60 nm thick LSM film with current collectors 50 μm apart. Both linear (□) and semilog (Δ) plots are shown.

REFERENCES

(1) Minh, N. Q. *J. Am. Ceram. Soc.* **1993**, *76*, 563.

(2) Minh, N. Q. *Solid State Ionics* **2004**, *174*, 271.

(3) Minh, N. Q.; Takahashi, T. *Science and Technology of Ceramic Fuel Cells*; Elsevier: Amsterdam, **1995**.

(4) Singh, P.; Minh, N. Q. *Int. J. Appl. Ceram. Technol.* **2004**, *1*, 5.

(5) Singhal, S. C. *Solid State Ionics* **2000**, *135*, 305.

(6) Singhal, S. C. *Solid State Ionics* **2002**, *152-153*, 405.

(7) Singhal, S. C.; Kendall, K. *High-temperature Solid Oxide Fuel Cells: Fundamentals, Design and Applications*; Elsevier Science, **2003**.

(8) Steele, B. C. H.; Heinzel, A. *Nature* **2001**, *414*, 345.

(9) Lu, X.; Faguy, P. W.; Liu, M. *J. Electrochem. Soc.* **2002**, *149*, A1293.

(10) Handke, M.; Harrick, N. J. *Appl. Spectrosc.* **1986**, *40*, 401.

(11) Pushkarev, V. V.; Kovalchuk, V. I.; d'Itri, J. L. *J. Phys. Chem. B* **2004**, *108*, 5341.

(12) Li, C.; Domen, K.; Maruya, K.-i.; Onishi, T. *J. Am. Chem. Soc.* **1989**, *111*, 7683.

(13) Li, C.; Domen, K.; Maruya, K.-i.; Onishi, T. *J. Catal.* **1990**, *123*, 436.

(14) Hunt, A. T.; Carter, W. B.; Cochran, J. K. *Appl. Phys. Lett.* **1993**, *63* 266.

(15) Choi, Y. M.; Abernathy, H.; Chen, H.-T.; Lin, M. C.; Liu, M. L. *ChemPhysChem* **2006**, *7*, 1957.

(16) Wang, J. H.; Liu, M. L.; Lin, M. C. *Solid State Ionics* **2006**, *177*, 939.

(17) Choi, Y. M.; Mebane, D.; Lin, M. C.; Liu, M. L. *Chem. Mater.* **2006**, *submitted*.

(18) Monkhorst, H. J.; Pack, J. D. *Phys. Rev. B* **1976**, *13*, 5188.